Surface Analysis Hot Paper

DOI: 10.1002/anie.201406455

Using Surface Segregation To Design Stable Ru-Ir Oxides for the Oxygen Evolution Reaction in Acidic Environments**

*Nemanja Danilovic, Ramachandran Subbaraman, Kee Chul Chang, Seo Hyoung Chang, Yijin Kang, Joshua Snyder, Arvydas Paul Paulikas, Dusan Strmcnik, Yong Tae Kim, Deborah Myers, Vojislav R. Stamenkovic, and Nenad M. Markovic**

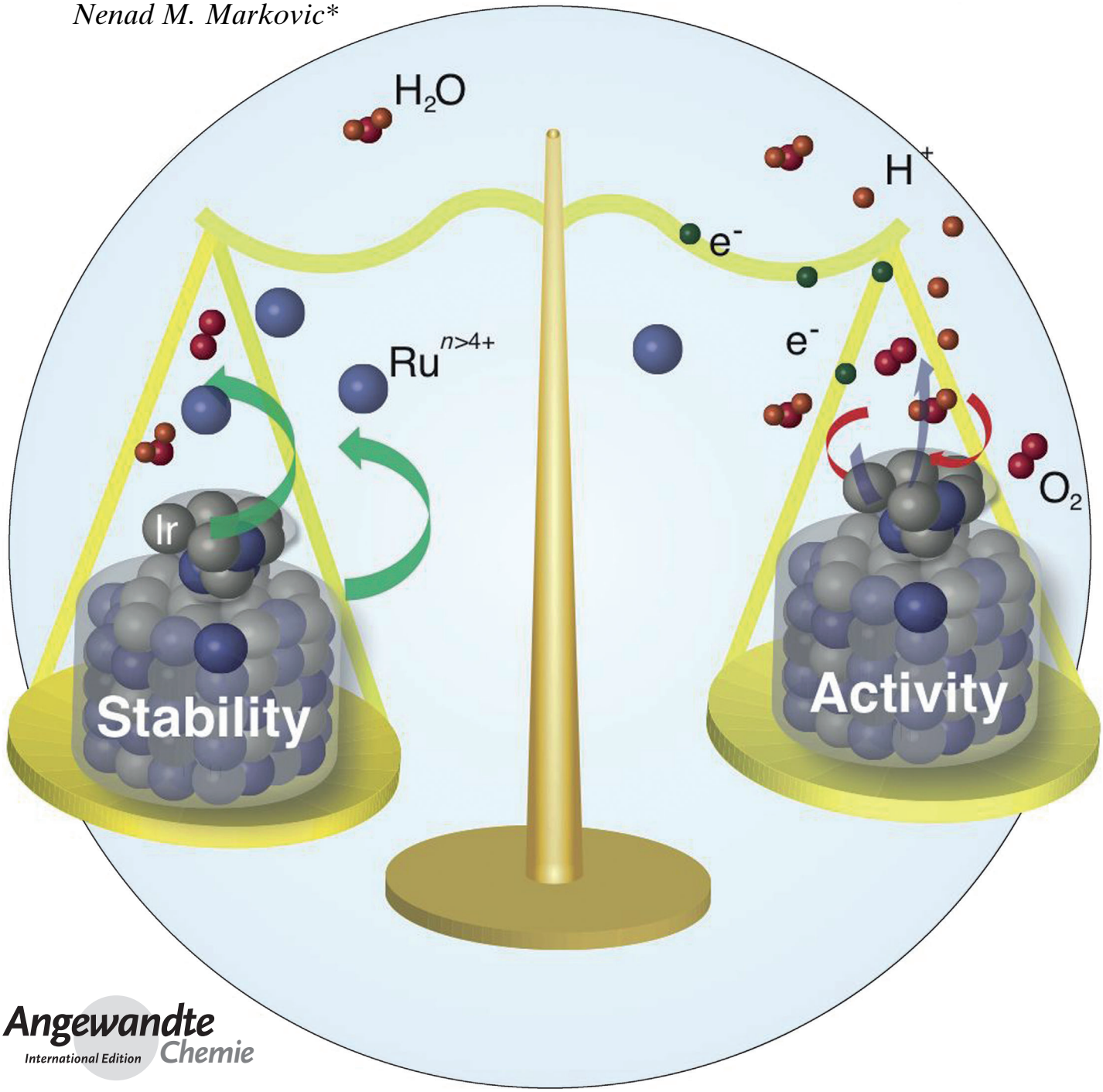

Abstract: *The methods used to improve catalytic activity are well-established, however elucidating the factors that simultaneously control activity and stability is still lacking, especially for oxygen evolution reaction (OER) catalysts. Here, by studying fundamental links between the activity and stability of well-characterized monometallic and bimetallic oxides, we found that there is generally an inverse relationship between activity and stability. To overcome this limitation, we developed a new synthesis strategy that is based on tuning the near-surface composition of Ru and Ir elements by surface segregation, thereby resulting in the formation of a nanosegregated domain that balances the stability and activity of surface atoms. We demonstrate that a $Ru_{0.5}Ir_{0.5}$ alloy synthesized by using this method exhibits four-times higher stability than the best Ru-Ir oxygen evolution reaction materials, while still preserving the same activity.*

The identification of materials for efficient energy conversion and fuel production in electrochemical systems must be guided by two equally important fundamental properties: optimization of their catalytic behavior and their long-term stability in hostile electrochemical environments.[1–3] This is especially true for the oxygen evolution reaction (OER), the anodic-half cell reaction that takes place at high overpotentials on oxidized metal surfaces in hydrogen–oxygen electrolyzers, metal–air batteries, and electrometallurgy.[2,4–6] Although the OER is a rather complex reaction, a combined set of experimental and theoretical trends based analyses has nonetheless emerged and provided the key catalytic factor that underlies the activity of OER catalysts: the binding energy between the substrate and the reactants, intermediates, and products.[4,7–12] In many respects, the understanding of the stability (e.g. dissolution/corrosion of catalysts at constant overpotential for the OER) of oxide materials, particularly at the atomic scale, during the OER is much less advanced, even for Ru-Ir alloys that are currently considered to be one of the most stable anode materials in proton-exchange membrane (PEM) based electrolyzers.[13–17] This is due to the long-standing difficulty associated with developing in situ methods that are capable of monitoring relationships between the potential-dependent variations in both the near-surface composition of the alloying component as well as the valence state of the Ru and Ir atoms as it relates to their stability in hostile electrochemical environments. Here, we show that this intrinsic disparity in understanding has a tendency to mask the inherently close ties that exist between the stability and activity of Ru-Ir alloy OER catalysts. By focusing on functional links between activity and stability, we were able to synthesize Ru-Ir nanostructured materials that exhibit stability four times that of the state-of-the art Ru-Ir catalysts while maintaining the high intrinsic activity for the OER.

Although the catalytic activity of Ru-Ir systems has been explored for decades,[18–23] there are few investigations of well-characterized alloys that can provide the foundation for any predictive ability when synthesizing tailored oxides with optimized reactivity and stability. To overcome this limitation we have developed a distinctive experimental strategy that is based on utilizing the surface segregation phenomenon that is capable of balancing the near-surface composition in such a way that the stability of surface atoms is enhanced without compromising the OER activity. Five $Ru_{1-x}Ir_x$ extended alloys were synthesized (see the Experimental Section for details) and characterized before and after annealing in ultrahigh vacuum (UHV). The surface compositions of oxygen-free, as-sputtered and thermally annealed alloys were determined by utilizing low-energy ion scattering (LEIS), while the bulk composition was assessed with X-ray photoelectron spectroscopy (XPS). As summarized in Figure 1 a, the surface and bulk compositions of as-sputtered alloys are essentially identical, as is expected since Ru and Ir have similar sputter cross-sections. Figure 1 a also reveals that annealing of the as-sputtered surfaces induces surface enrichment of Ir atoms, a phenomenon that can be accounted for by the lower heat of sublimation of Ir.[24] Figure 1 b shows that the alloy with an *hcp* bulk lattice (>50 at % Ru) exhibits a more pronounced segregation than the *fcc* alloys (<50 at % Ru), but the outermost layer is not completely enriched by Ir, even in the *hcp* alloy. For example, in the case of the $Ru_{0.5}Ir_{0.5}$ alloy, the surface composition of Ir is approximately 75 at %, while the concentration profile of Ir monotonically decreases until the bulk atomic composition is reached (Figure 1 c). Such a nanosegregated structure offers a unique opportunity to determine the functional links between the stability of the alloy oxides and activity for the OER.

An optimal relationship between stability and reactivity is found with $Ru_{0.5}Ir_{0.5}$, therefore, only the results for this alloy will be presented and discussed (summarized in Figure S2 in the Supporting Information). The activity for the OER (expressed as measured overpotentials at $5\,mA\,cm^{-2}$) together with the data for the stability of these oxides during the OER, expressed as the quantifiable dissolution of metal cations (using ICP-MS) during a 10 min galvanostatic hold at 1.6 V, are summarized in Figure 2. Two types of $Ru_{0.5}Ir_{0.5}$ oxides with strikingly different morphologies were

[*] Dr. N. Danilovic, Dr. R. Subbaraman, Dr. K.-C. Chang, Dr. S. H. Chang, Dr. Y. J. Kang, Dr. J. Snyder, Dr. A. P. Paulikas, Dr. D. Strmcnik, Dr. V. R. Stamenkovic, Dr. N. M. Markovic
Materials Science Division, Argonne National Laboratory
9700 Cass Ave, Argonne, IL 60439 (USA)
Prof. Y.-T. Kim
Pusan National University
30 Jangjeon-dong, Geumjeong-gu, Busan 609-735 (Korea)
Dr. D. Myers
Chemical Science and Engineering Division
Argonne National Laboratory
9700 Cass Ave, Argonne, IL 60439 (USA)

[**] This work was supported by the US Department of Energy, Basic Energy Sciences, Materials Sciences and Engineering Division. Microscopy studies were accomplished at the Center for Nanophase Materials Sciences at Oak Ridge National Laboratory, which is sponsored by the Scientific User Facilities Division, Office of Basic Energy Sciences, US Department of Energy, and at the Electron Microscopy Center (ANL). The use of the Advanced Photon Source and Center for Nanoscale Materials was supported by the US Department of Energy, Office of Science, Office of Basic Energy Sciences, under Contract No. DE-AC02-06CH11357.

Supporting information for this article is available on the WWW under http://dx.doi.org/10.1002/anie.201406455.

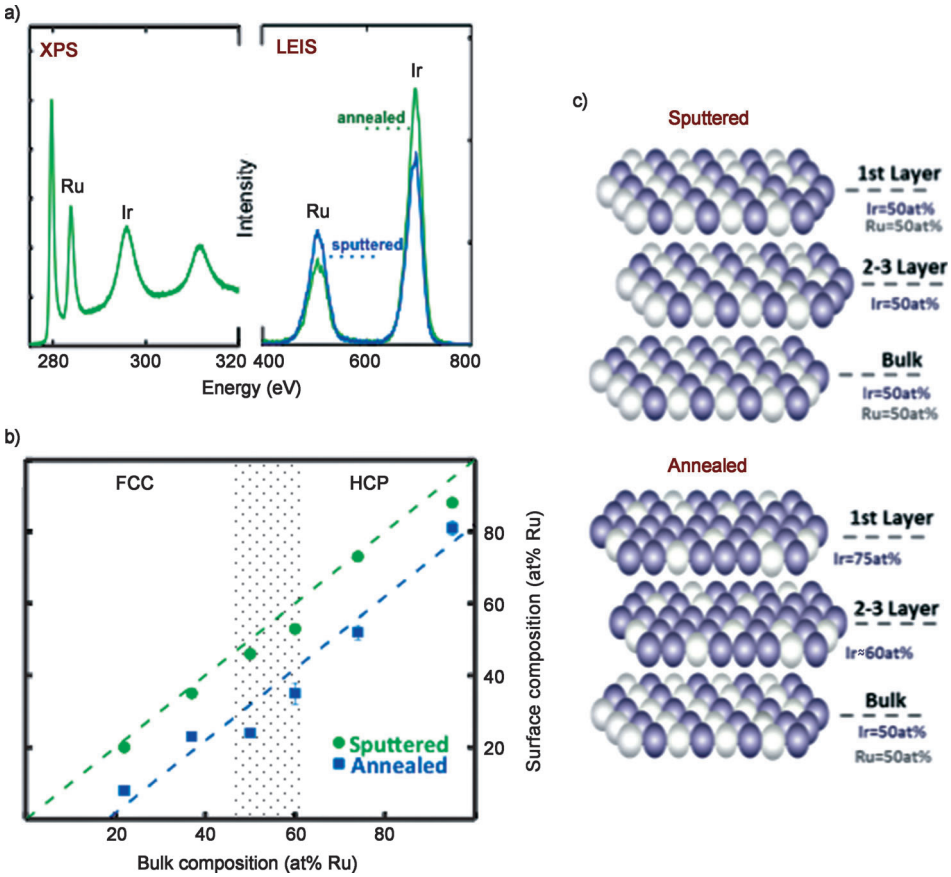

Figure 1. UHV preparation and characterization of the nano-segregated $Ru_{1-x}Ir_x$ near-surface composition of bulk electrodes. a) Representative LA-XPS and LIES spectra used to quantify the bulk and surface composition of UHV sputtered and annealed $Ru_{1-x}Ir_x$ electrodes, respectively. b) Ru surface and bulk compositions of sputtered and annealed $Ru_{1-x}Ir_x$ alloys as determined by LA-XPS and LEIS for the sputtered (green circles) and annealed (blue squares) electrodes; and c) Schematic representations of the $Ru_{0.5}Ir_{0.5}$ sputtered (top) and annealed (bottom) surface with the segregation-induced enrichment (ca. 75 at%) of Ir at the surface.

prepared: crystalline "thermal chemical" oxides (TC-oxide) grown by thermal O_2 exposure of the metal samples, and highly defective amorphous electrochemical oxides (EC-oxide) involving hydroxy and related species in "hydrous oxides" formed by water electrooxidation at high anodic potentials (see Figure S3 in the Supporting Information). Three noteworthy features can be identified from Figure 2 (see CVs in Figure S4 in the Supporting Information). First, Figure 2 shows that the overpotential for the OER is higher for both the crystalline TC-oxides and thermally annealed/nanosegregated electrodes than for the corresponding amorphous EC-oxides and as-sputtered electrodes. Second, the upper part of Figure 2 reveals that the solution concentration of Ru is always much higher than that of Ir, which indicates preferential dissolution of Ru. Third, irrespective of the nature of the oxide, annealed alloys with the nanosegregated profile are always more stable but less active than sputtered samples. These results suggest that there is an inverse relationship between activity and stability, as seen previously for strontium ruthenate OER catalysts,[16] where the activity is related to the density of defects/low-coordinated surface atoms either initially present on the sputtered surfaces and amorphous electrochemical oxides, or those created through dissolution of high oxidation state cations at OER potentials, typically Ru sites. Defects, however, are the source of the instability of these oxide surfaces, as demonstrated through ICP-MS and XANES analysis.

To further investigate these relationships, in situ X-ray near edge structure analysis (XANES) was used to establish variations in the valence state *n* of Ru and Ir during the positive potential scan from 0.05 V to 1.45 V. To ensure that the potential-dependent changes in the oxidation state of the near-surface oxide before and during the OER were not influenced by the contribution from the valence states of bulk metallic atoms, XANES experiments were performed on thin (ca. 1–5 nm) films of Ru-Ir alloy deposited on glassy carbon substrates. We mention in passing that although it is not possible to unambiguously determine the exact value of the surface oxidation state of Ru and/or Ir, it is indeed conceivable to determine the average oxidation state in

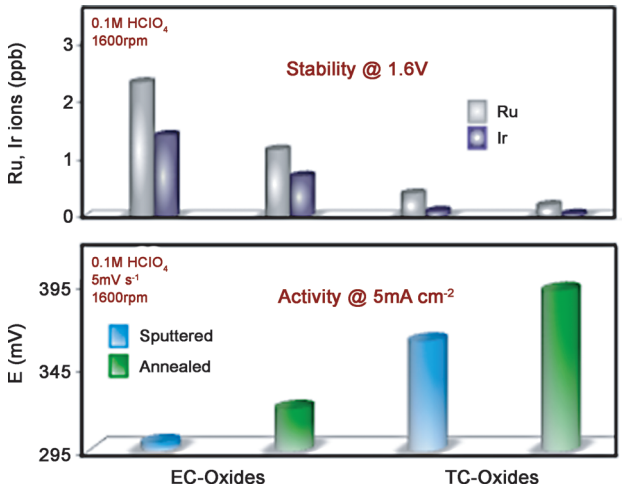

Figure 2. Relationships between the activity and stability of sputtered and annealed $Ru_{0.5}Ir_{0.5}$ EC- and TC-oxides during OER. Relationships between the activity and stability for sputtered (blue bars) and annealed (green bars) $Ru_{0.5}Ir_{0.5}$ alloys prepared either as EC-oxides or TC-oxides. EC-oxides are always more active but less stable, thus signaling a strong inverse relationship between activity and stability. While activity on annealed nanosegregated surface is reduced by 10%, the stability is enhanced fourfold.

the near-surface region. Furthermore, at a given electrode potential, the valence state of Ru and Ir may not differ significantly (see below); therefore, the XANES data are summarized as a normalized "effective oxide thickness" (see Section V in the Supporting Information). In Figure 3, there

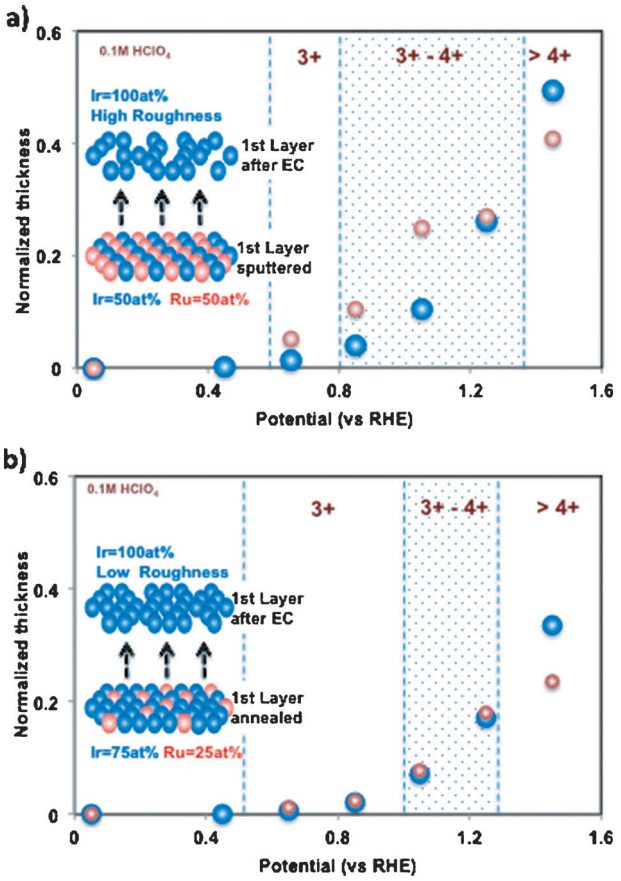

Figure 3. Relationships between the surface oxidation state of sputtered and annealed $Ru_{0.5}Ir_{0.5}$ with Ir skeleton formation during OER. The potential-dependent changes in the valence states of sputtered (a) and annealed (b) $Ru_{0.5}Ir_{0.5}$, as determined from XANES analyses. The unique behavior is that above 1.45 V a much higher "normalized effective thickness" of Ir oxide with a $n>4+$ state is observed, thus suggesting the formation of Ir skeleton (see schematic models of the sputtered and annealed surfaces).

are several significant features that are important to emphasize. First, on as-sputtered thin films, Ru and Ir are found to be in the zero-valence state ($n=0$) between 0.05 and 0.6 V, which implies that reversible adsorption of hydroxy species at this potential has no significant effect on the oxidation state of the Ru and Ir. Above 0.8 V, however, the valence state systematically changes from $n=0$ to $n=3+$ at $0.6<E<0.9$ V, to mixtures of $n=3+$ and $n=4+$ at $0.9<E<1.3$ V, to $n=4+$ at $1.3<E<1.45$ V, and, finally, to $n>4+$ (but not $5+$, $6+$, or $8+$) for $E>1.45$ V. Qualitatively, a similar "oxidation shift" is observed for the annealed thin films (Figure 3b); for example, the transition from $n=0$ to a mixture of $n=3+$ and $4+$ just above 0.8 V is followed first by a transition to the "pure" $n=4+$ oxidation state and above 1.4 V to $n>4+$. However, Figure 3 reveals that, quantitatively, there are substantial differences in the effective oxide thickness for these two elements. First, although the effective oxide thickness of as-sputtered films below 0.3 V is much lower for the nobler Ir than the highly oxophilic Ru, there is no measurable difference in the effective oxide thickness between these two elements in the case of annealed films. This difference can be accounted for by the segregation-induced increase in the near-surface concentration of Ir, as well as by the ordering of surface atoms—a well-established UHV protocol for removal of the surface defects present in an as-sputtered thin film. Second, the effective oxide thickness for the thermally annealed films is always reduced relative to that of the as-sputtered films, thus indicating an overall lower oxophilicity of the thermally annealed surfaces. Third, independent of the nature of electrode preparation, there is a much higher normalized effective thickness of Ir oxide with the $n>4+$ state than Ru oxide, which is opposite from the behavior observed with pure Ru and Ir electrodes.[17] Consistent with a rapid loss of the near-surface Ru atoms shown in Figure 2, it is apparent that Ru atoms are less stable than Ir atoms, and therefore dissolve quickly, leaving behind a more "noble" Ir skeleton layer with 100 at% Ir at the surface (see schematic model in Figure 3b). In turn, this implies that Ru "stabilization" by Ir is governed by protection of the buried, less-noble Ru atoms by the Ir skeleton rather than by any change in the electronic properties of Ru induced by the presence of Ir, as frequently proposed in the literature[22] (see Figures S10–S13 in the Supporting Information). Finally, although the Ir skeleton is formed with both as-sputtered and thermally annealed surfaces, the microscopic structures of these two surfaces are rather different, the latter being more ordered (fewer defects and less porous), as schematically shown in Figure 3b.

Controlling the segregation-induced enrichment and ordering of Ir in the Ru-Ir alloy, as demonstrated by our results, is a potentially useful strategy for optimizing the activity and stability of bimetallic alloy OER catalysts. We tested the viability of this strategy by synthetizing nanoparticles that mimic the nanosegregated structures presented above. The synthesis of real-world anode catalysts must embrace two important steps: segregation-induced formation of the Ir skeleton followed by thermal oxidation of such structures. Colloidal synthesis was used to create homogeneous, bulk-like $Ru_{0.5}Ir_{0.5}$ alloy nanoparticles (see Experimental Section for procedure) that were subsequently annealed in Ar/H_2 to induce surface enrichment and ordering of Ir. Both the homogeneous and nanosegregated nanoparticles were then subjected to oxidation for comparison with commercial $Ru_{0.5}Ir_{0.5}O_2$ nanocatalysts. Transmission electron microscopy (TEM) revealed that the well-dispersed $Ru_{0.5}Ir_{0.5}O_2$ catalysts have nearly identical cubo-octahedral shapes and a particle size distribution centered in the 5–10 nm range. The distribution of Ru and Ir within the nanoparticle was determined using energy-dispersive X-ray spectroscopy (EDX; Figure 4, upper part), where the annealed and thermally oxidized nanoparticles clearly exhibit a surface enrichment of Ir, similar to the bulk and thin-film electrodes, whereas the un-annealed and oxidized nanoparticles contain a homogeneous distribution of Ru and Ir. This demonstrates

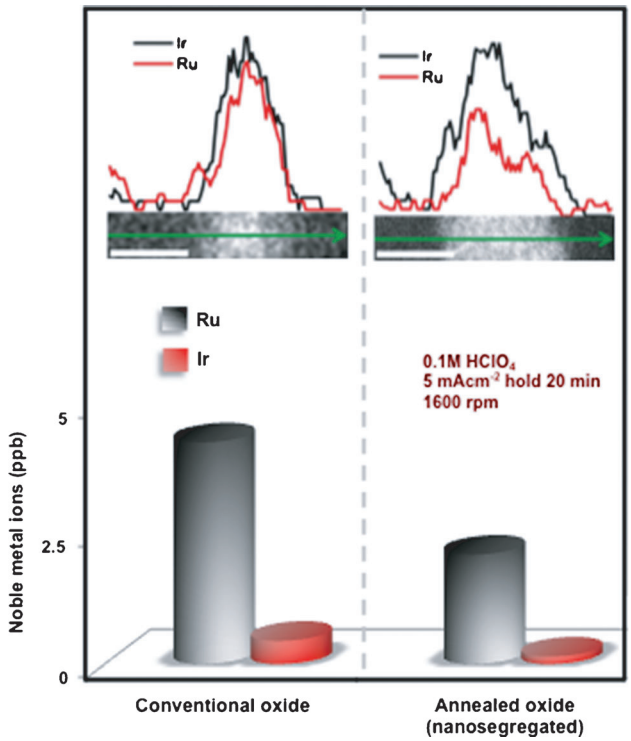

Figure 4. From model to real nanosegregated $Ru_{0.5}Ir_{0.5}O_2$ systems. Top: Energy-dispersive X-ray spectroscopy (EDX) used to determine the elemental distribution of Ru and Ir within the nanoparticle. While the as-prepared, conventional oxide nanoparticle exhibits a uniform Ru/Ir profile, the preannealed and then oxidized $Ru_{0.5}Ir_{0.5}$ nanoparticle reveals the segregation-induced enrichment of Ir in the near-surface region. The white scale bars represent 2 nm dimension. Bottom: Measured Ru and Ir cations in a solution produced during the OER (current held at 5 $mA\,cm^{-2}$; duration time 20 min). For the same current density and electrode potential, Ir nanosegregated skeleton is four-times more stable than conventional oxide nanoparticles.

that the annealing step is critical for forming a surface-segregated alloy, and suggests that the annealed nanoparticles may be able to preserve the increased reactivity and stability properties observed in the nanosegregated thin-film samples. Indeed, we find that although the activities of nanosegregated and homogeneous nanoparticles are nearly identical, the stability of the surface-enriched alloy nanoparticles is nearly 3–4 times higher than their homogeneous counterparts (lower part of Figure 4).

In conclusion, we showed that the activity of oxide materials for the OER is primarily controlled by the stability of surface atoms rather than the energy of adsorption of reaction intermediates. A practical consequence of such a close relationship between activity and stability is that the best materials for the OER should balance the stability and activity in such a way that the dissolution rate is neither too fast nor too slow. For the Ru-Ir system, this requirement is realized by employing the power of surface segregation to form a nanosegregated "Ir-protective skeleton" that is four times more stable, but equally as active, as the commercial real-world Ru-Ir alloy anode catalysts.

Experimental Section

Bulk electrode preparation: Bulk metal and alloy electrodes, obtained from ACI alloys (cylindrically shaped, 6 mm diameter, 4 mm thick, 99.99 % pure materials), were ground and polished down to 0.05 μm alumina powder (Buehler powders and grinding paper). This procedure was repeated when needed, such as after excessive dissolution or thermal oxidation. The bulk electrodes were subsequently annealed in UHV (described below) or in a RF furnace (producing comparable results) in Ar/3 % H_2 for 5 min at 1100 °C. "Sputtered" bulk electrodes were prepared in a UHV (described below). Thermal oxides were prepared by first annealing them in Ar/3 % H_2 as described above, then subsequently annealing them in the RF furnace in pure O_2 at 600 (pure Ru), 700 (Ru-Ir alloys), and 800 °C (pure Ir) for 5 min.

Thin-film electrode preparation: Thin films were prepared by magnetron sputter deposition onto Ti (6 mm diameter, 4 mm thick, ACI alloys, 99.99 % pure) and glassy carbon (GC) disks in a sputter deposition chamber (AJA International, Inc.) with a nominal base pressure of 4×10^{-10} Pa equipped with both radio-frequency (RF) and direct-current (DC) power supplies. Both the Ti and GC disks were polished with 0.05 μm alumina powder (Buehler) on microcloth polishing pads (Buehler) then rinsed and sonicated in Millipore water. Prior to deposition of the metal films, the substrates were cleaned with RF Ar plasma for 4 min (25 W RF, 0.2 Pa Ar). As-deposited films were removed from the sputter chamber protected by a drop of Millipore water and transferred to a tube furnace (Carbolite) where the films were annealed under a controlled atmosphere, or stored for XAS experiments. For XAS experiments, the samples were sputtered to the following thickness Ir 1 nm, $Ru_{0.5}Ir_{0.5}$ 2 nm, and Ru: 5 nm, because of experimental constraints (see the Supporting Information for details). Annealed films were produced by annealing in a tube furnace for 1 h at 350 °C in Ar/3 % H_2; these conditions were found to elicit the same surface enrichment without affecting the Ti substrate. The temperature for annealing was confirmed by performing LEIS to analyze the evolutions of surface composition with time. Furthermore, the films were verified electrochemically to produce comparable activities and stabilities as bulk alloys.

Nanoparticle synthesis**:** Nanoparticles were synthesized under an argon flow. $[Ru(acac)_3]$ (0.1 mmol) and $[Ir(acac)_3]$ (0.1 mmol) were dissolved in oleylamine (10 mL) and benzyl ether (5 mL). The formed solution was heated to 180 °C. Once the temperature of the solution in the reaction flask reached 180 °C, 1M superhydride (1 mL) was injected into the reaction flask. The reaction temperature was further increased to 240 °C and kept at 240 °C for 30 min. After reaction, the solution was allowed to cool. The product was precipitated by ethanol and then redispersed in hexane. The nanoparticles were then dispersed onto Ti or GC disks, heated in a tube furnace to 200 °C for 2 h to evaporate the surfactant, then oxidized in a pure O_2 atmosphere at 350 °C for 1 h to obtain "as-sputtered", i.e. conventional bulk oxide. To obtain an annealed (surface-segregated Ir) oxide the metal nanoparticles were heated to 400 °C in Ar/5 % H_2 for 1 h prior to the oxidation treatment discussed above; this temperature was optimal in producing the Ir segregation, as confirmed by TEM characterization.

Electrochemical characterization**:** After electrode preparation (described above) the surface was protected with a drop of deionized water (DIW), embedded into a rotating disk (RDE), and transferred to a standard three-compartment electrochemical cell containing 0.1M $HClO_4$ (Sigma Aldrich). The electrodes were always immersed under potential control, at 0.05 V (CV or XAS) or 1.23 V (OER measurements) in a solution saturated with Ar (identical OER results were obtained in O_2, without affecting the activity or stability measurements). The sweep rate for the CV measurements was 50 $mV\,s^{-1}$, while for potentiodynamic (OER) measurements the sweep rate was 5 $mV\,s^{-1}$ at a rotation rate of 1600 rpm. Potentiodynamic and potentiostatic experiments were obtained with iR compensation,

typically 18 Ohms. An Ag/AgCl reference electrode and Pt counter electrode were used in all experiments; all reference potentials are corrected to the reversible hydrogen electrode (RHE) scale. Note, no Pt was detected in the solution after OER experiments (ICP measurements) or on the surface of the electrodes (XPS), which indicates there was no dissolution of the counter electrode during experiments (if this did happen it would be detrimental to OER performance because of the much lower activity of Pt).

Ultrahigh vacuum characterization**:** XPS (X-ray photoemission spectroscopy) measurements were done in an Omicron UHV (ultrahigh vacuum) system having a base pressure of low 10^{-11} Torr. Specimens were illuminated with monochromatized aluminum k-α radiation of 1.486 keV photon energy. The photoemitted electrons were directed into a hemispherical energy analyzer where their flux was measured as a function of their energy. The resulting spectrum was a signature of the atomic composition of the near-surface (about two nm deep) region of the specimen. Specimens were usually examined after cleaning in situ in UHV; sometimes they were examined as prepared, without being cleaned. Cleaning in UHV consisted of multiple cycles of sputtering with 1 keV argon ions followed by heating to 850 °C. After cleaning, nothing but ruthenium and/or iridium spectra were observable by XPS.

LEISS (low-energy ion-scattering spectroscopy) measurements were done in an Omicron UHV (ultrahigh vacuum) system having a base pressure of low 10^{-11} Torr. Specimen surfaces were irradiated with a beam of either helium ions or neon ions; the energy of the scanning ions was 1.0 keV. Those backscattered ions that had a fixed geometrical relation to the irradiating beam were directed into a hemispherical energy analyzer where their flux was measured as a function of their energy. The resulting spectrum was a signature of the composition of the outermost single atomic layer of the specimen's surface. Specimens were examined after cleaning in situ in UHV. Cleaning in UHV consisted of multiple cycles of sputtering with 1 keV Ar^+ ions followed by heating to 850 °C. Specimens were examined after a final sputtering step or after a final heating step to observe changes in the composition of the outermost atomic layer.

X-ray absorption spectroscopy (XAS)**:** The XAS data were acquired at bending magnet beamline 12-BM-B at the Advanced Photon Source (APS), Argonne National Laboratory. The beamline uses a double-crystal Si(111) monochromator to define the incident X-ray energy and a double-mirror system for horizontal beam focusing and harmonic rejection. A custom made in situ electrochemical X-ray cell with a Ag/AgCl reference electrode was mounted vertically to minimize elastic scattering intensity and to better match the focused beam shape. X-ray absorption spectroscopy (XAS) was taken in the fluorescence mode with a 13 element Ge detector (Oxford). The energy was calibrated by using Ru and Ge foils. The electrode potential and solution volume above the sample were maintained in a way so as not to interfere with the XAS measurements or the electrochemical surface. To summarize and compare the oxidation of the different samples, an "effective oxide thickness" was utilized, which is the oxide fraction normalized by the film thickness. For more information regarding these measurements, please see the Supporting Information.

Inductively coupled plasma mass spectrometry (ICPMS)**:** A PerkinElmer/SCIEX ELAN DRC-II spectrometer was used for solution analysis. The ICP samples were obtained by sampling the electrolyte prior to any decreases in potential to prevent re-deposition of dissolved products.

Electron microscopy**:** STEM and elemental analysis (line-scan) were carried out on a JEOL 2200FS TEM/STEM system with a CEOS aberration (probe) corrector. The microscope was operated at 200 kV in HAADF-STEM mode equipped with a Bruker-AXS X-Flash 5030 silicon drift detector.

X-ray diffraction**:** XRD measurements were made using a rotating anode X-ray generator (Rigaku, Rotaflex, RTP 300 RC) with CuKα target ($\lambda = 1.54$ Å) and doubly bent pyrolytic graphite monochromator for point focusing. Samples were transferred to the XRD directly after preparation in air.

Received: June 23, 2014
Revised: August 8, 2014
Published online: October 8, 2014

Keywords: iridium · oxides · oxygen evolution reaction · ruthenium · surface chemistry

[1] J. Greeley, N. M. Markovic, *Energy Environ. Sci.* **2012**, *5*, 9246 – 9256.
[2] D. K. Kinoshita, *Electrochemical Oxygen Technology*, Wiley, **1992**.
[3] W. Vielstich, H. Yokokawa, H. A. Gasteiger, *Handbook of Fuel Cells: Fundamentals Technology and Applications. Advances in Electrocatalysis, Materials, Diagnostics and Durability: Part 1*, Wiley, Hoboken, **2009**.
[4] S. Trasatti, *Electrochim. Acta* **1984**, *29*, 1503 – 1512.
[5] M. Tatsumisago, M. Wakihara, T. Minami, C. Iwakura, S. Kohjiya, I. Tanaka, *Solid State Ionics for Batteries*, Springer, Heidelberg, **2006**.
[6] M. Armand, J.-M. Tarascon, *Nature* **2008**, *451*, 652 – 657.
[7] J. Suntivich, K. J. May, H. A. Gasteiger, J. B. Goodenough, Y. Shao-Horn, *Science* **2011**, *334*, 1383 – 1385.
[8] J. O. Bockris, T. Otagawa, *J. Phys. Chem.* **1983**, *87*, 2960 – 2971.
[9] Y. Matsumoto, E. Sato, *Mater. Chem. Phys.* **1986**, *14*, 397 – 426.
[10] J. Rossmeisl, A. Logadottir, J. K. Nørskov, *Chem. Phys.* **2005**, *319*, 178 – 184.
[11] S. Ardizzone, G. Fregonara, S. Trasatti, *Electrochim. Acta* **1990**, *35*, 263 – 267.
[12] D. Galizzioli, F. Tantardini, S. Trasatti, *J. Appl. Electrochem.* **1974**, *4*, 57 – 67.
[13] T. Reier, M. Oezaslan, P. Strasser, *ACS Catal.* **2012**, *2*, 1765 – 1772.
[14] S. Park, Y. Shao, J. Liu, Y. Wang, *Energy Environ. Sci.* **2012**, *5*, 9331.
[15] Y. Lee, J. Suntivich, K. J. May, E. E. Perry, Y. Shao-Horn, *J. Phys. Chem. Lett.* **2012**, *3*, 399 – 404.
[16] S. H. Chang, N. Danilovic, K.-C. Chang, R. Subbaraman, A. P. Paulikas, D. D. Fong, M. J. Highland, P. M. Baldo, V. R. Stamenkovic, J. W. Freeland, et al., *Nat. Commun.* **2014**, *5*, 4191.
[17] N. Danilovic, R. Subbaraman, K.-C. Chang, S. H. Chang, Y. J. Kang, J. Snyder, A. P. Paulikas, D. Strmcnik, Y.-T. Kim, D. Myers, et al., *J. Phys. Chem. Lett.* **2014**, *5*, 2474 – 2478.
[18] M. H. Miles, E. A. Klaus, B. P. Gunn, J. R. Locker, W. E. Serafin, S. Srinivasan, *Electrochim. Acta* **1978**, *23*, 521 – 526.
[19] S. Trasatti, G. Buzzanca, *J. Electroanal. Chem. Interfacial Electrochem.* **1971**, *29*, A1 – A5.
[20] L. I. Krishtalik, *Electrochim. Acta* **1981**, *26*, 329 – 337.
[21] R. Kötz, H. J. Lewerenz, P. Bruesch, S. Stucki, *J. Electroanal. Chem. Interfacial Electrochem.* **1982**, *150*, 209 – 216.
[22] R. Kötz, S. Stucki, *Electrochim. Acta* **1986**, *31*, 1311 – 1316.
[23] R. Kötz, S. Stucki, *J. Electrochem. Soc.* **1985**, *132*, 103 – 107.
[24] A. V. Ruban, H. L. Skriver, J. K. Nørskov, *Phys. Rev. B* **1999**, *59*, 15990.

